Sound transmission through a periodic acoustic metamaterial grating

Xiang Yu [a], Zhenbo Lu [b], Tuo Liu [c], Li Cheng [c], Jie Zhu [c], Fangsen Cui [a, *]

[a] Institute of High Performance Computing, A*STAR, Singapore, 138632, Singapore
[b] Temasek Laboratories, National University of Singapore, Singapore, 117411, Singapore
[c] Department of Mechanical Engineering, The Hong Kong Polytechnic University 999077, Hong Kong

ARTICLE INFO

ABSTRACT

This study investigates into the sound transmission through a periodic acoustic metamaterial grating of finite size. The single-layer grating is constructed by periodically arranging sub-wavelength unit cells in a slab, as a part of a large baffle between two acoustic domains. The metamaterial unit cell consists of an open duct decorated with coiled resonators, which intends to suppress sound transmission using its acoustic stop-band. The space-coiling structure allows the metamaterial to operate at low frequency with a compact size. Analytical approach to predict the sound transmission loss (STL) of the combined baffle is developed, which is employed to study its sound attenuation under normal and oblique incidence. Results show that the unit cell geometry, the periodicity of grating elements, and the angle of incidence significantly affect the STL. The STL behavior of the acoustic grating is mainly governed by three physical effects, including the acoustic stop-band, the edge diffraction, and the destructive radiation interference behind the acoustic grating. Detailed mechanism studies for these effects are discussed using numerical examples. Experiment is conducted to validate the proposed numerical approach. This paper presents a theoretical framework to predict and study the performance of acoustic gratings comprised of metamaterial unit cells, which can be further extended to study phase tailoring acoustic metasurface.

© 2019 Elsevier Ltd. All rights reserved.

1. Introduction

Acoustic metamaterials are a type of artificial materials that are designed to provide exotic properties absent in nature. The study of using acoustic metamaterials to manipulate sound wave propagation has received much attention, particularly for the purpose of low-frequency absorption and isolation beyond the restriction of dimension and weight [1–3]. For example, the initial realization by incorporating metal spheres in soft silicone epoxy exhibits negative dynamic mass, which leads to strong elastic wave attenuation [4]. The membrane-type acoustic metamaterial uses a simple and compact construction to realize a resonance system with negative dynamic mass [5]. The metamaterial based on Helmholtz resonators demonstrates negative modulus which induces deep sub-wavelength sound isolation [6]. In contrast to the Bragg scattering sonic crystals whose lattice constant is usually on the order of half wavelength [7], the idea of metamaterials is to take the advantage of

* Corresponding author. Institute of High Performance Computing, A*STAR, Singapore, 138632, Singapore.
E-mail address: cuifs@ihpc.a-star.edu.sg (F. Cui).

locally resonant systems to control sound wave on a sub-wavelength scale. This could potentially overcome the limitation of bulky structures for noise control in audible frequency regime and could substantially innovate novel acoustic applications.

Several types of locally resonant systems can be used as the basic unit cell of an acoustic metamaterial. For example, the membrane-type metamaterial uses a concentrated mass attached to a membrane to behave like a spring-mass-damper system, thus generating sub-wavelength sound transmission [8–10] and absorption [11]. The periodic Helmholtz resonator array isolates sound at the ultra-low frequency range by using the transmittance stop-band generated by local resonance [6]. The Mie-resonator [12] and split tube resonator [13] can be viewed as variations of Helmholtz resonator which showed significant sub-wavelength feature. These examples demonstrate the deep sub-wavelength property of metamaterial with extremely compact geometry, but practical sound control is often preferable over a broad band of frequencies, being incompatible with the resonance-based metamaterials. This calls for a balance between the sub-wavelength property and the broadband performance.

Acoustic metasurfaces are a newer class of acoustic metamaterials which have surface profile and sub-wavelength thickness, allowing on-demand tailoring of sound propagation by imposing a specific boundary. The study in this category starts with an attempt to arbitrarily steer transmitted or reflected wavefront by introducing phase shifts to the incident waves [14,15]. The wavefront modulation is a diffractive phenomenon governed by phase control, and later on, the metasurface is broadened to the traditional categories of sound absorption [11,16], where the constituting unit cells can be identical without possessing phase difference. An attempt to realize an ultra-sparse metasurface for both sound isolation and air ventilation was made by using artificial Mie resonators [12], but the demonstrated insertion loss was low due to the low filling ratio.

The class of metamaterial unit with an acoustic duct can be utilized for sound isolation without completely blocking air ventilation. The duct allows air passage while the resonators attached to the side-branch can provide attenuation effect on the sound transmission. For example, a two-dimensional array of low loss cylindrical cavities was studied, showing negative bulk modulus and dispersion relation of acoustic bands [17]. The resonant tubular array demonstrated continuous tuning of compressibility in a wide range [18]. A sub-wavelength acoustic panel based on resonant ducts was constructed to provide high sound absorption using accumulation of resonances [19,20]. Conceptually, the ensemble of duct and attached resonators can be considered as a metamaterial unit cell. If we periodically arrange such unit cells in a slab, an *acoustic grating* can be constructed to realize special acoustic functions by making use of the unusual property of the unit cells and also the interaction between the unit cells. Here, the acoustic grating is viewed as a subclass of acoustic metasurface where the constituting unit cells are identical rather than possessing a certain phase relationship. As the thickness of a single-layer acoustic grating equals to that of the constituting element, the slab structure has excellent geometric advantage benefiting from the sub-wavelength size of the unit cells.

This study investigates into the sound transmission characteristics in a single-layer acoustic grating constructed by using metamaterial unit cells. The unit cell comprises a short acoustic duct decorated with an array of coiled resonators, forming a *duct-like* metamaterial. The unit cells are periodically arranged in a plane which is perpendicular to the sound propagation direction through the duct, as a part of a large baffle separating two acoustic domains. Particular interests will be paid to uncovering the effect of unit cell designs and their periodicity on the STL performance. We introduce a hybrid numerical model to predict the sound transmission of the system, where analytical method is used to model the incident and transmitted sound fields, and Finite Element Method (FEM) is used to model the metamaterial with complicated geometry. The proposed approach provides an accurate and effective tool to study the involved parameters and to uncover the physical aspects.

This paper is organized as follows: Sec. 2 describes the numerical approach which is specifically developed to model a baffled acoustic slab composed of metamaterial elements. The acoustic fields on both sides of the baffle are modeled analytically, and the connections via metamaterial unit cells are modeled as waveguides using the transfer matrix method. In Sec. 3, the one-dimensional acoustic transmission through a unit cell is first studied using a simplified impedance tube model. It is shown that the unit cell is a type of metamaterial possessing resonance-induced negative modulus. Its dispersion relation, effective material property and the layer effect are analyzed. Using the proposed numerical approach, Sec. 4 further analyzes the STL of the acoustic grating, particularly focusing on the effect of unit cell periodicity and sound incidence angle. Experimental test to validate the simulation result and the proposed numerical framework is presented in Sec. 5.

2. Numerical approach

Let us consider a two-dimensional slab comprised of a number of metamaterial unit cells arranged periodically, forming a single-layer grating as a part of a large baffle. The metamaterial unit cells are open acoustic ducts decorated with coiled resonators [21], as shown in Fig. 1. The boundaries of the unit cells and the separation between grating elements are assumed as rigid to simplify the theoretical modeling. Using the Cartesian coordinate system, let x-axis denote the slab normal and y-axis denote the slab tangential. The sound incidence angle α is defined relative to the slab normal, with $\alpha = 0°$ being normal incidence case and the $\alpha = 90°$ being the grazing incidence case.

Assuming the slab is excited by plane wave with incidence angle α, the incident sound pressure field on the left-hand side of the baffle can be expressed as [22]:
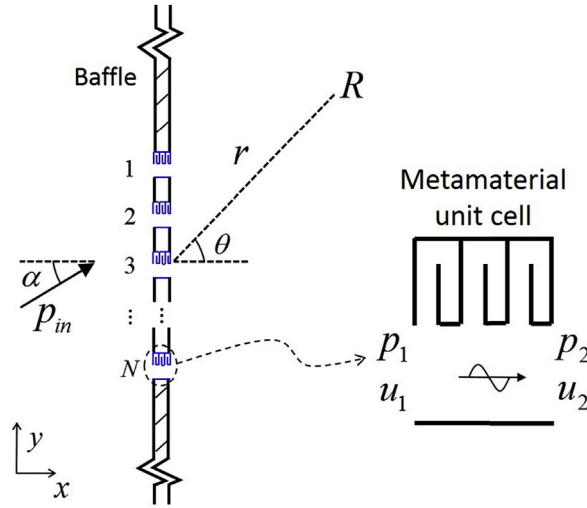
Fig. 1. A slab comprised of metamaterial unit cells arranged periodically to form a single-layer acoustic grating. The metamaterial unit cell is an open duct decorated with coiled resonators.

$$p_{in}(x, y, \omega) = p_0 e^{j(\omega t - kx \cos \alpha - ky \sin \alpha)}, \tag{1}$$

where p_{in} is the incident pressure field, p_0 is the amplitude of incident wave; $j = \sqrt{-1}$; k is the wave number $k = \omega/c_0 = 2\pi f/c_0$, ω is the angular frequency and c_0 is the speed of sound in air. At the slab interface where $x = 0$, the above expression reduces to $p_0 e^{j(\omega t - ky \sin \alpha)}$. The time dependence $e^{j\omega t}$ can be neglected if we carry out harmonic analysis.

On the right-hand side of the slab, the transmitted sound through the unit cell causes an air velocity disturbance at the outlet aperture and radiates into the receiving field. Under the baffled condition, sound radiation from the periodic outlet apertures can be modeled as cylindrical waves radiating into a semi-infinite free space, as illustrated in Fig. 2. To determine the radiation impedance between the radiated pressure field and the unit cell velocity, the governing Helmholtz equation is:

$$\left[\nabla^2 + k^2(\overrightarrow{r}) \right] p_{rad}(\overrightarrow{r}, \omega) = 0, \tag{2}$$

where p_{rad} is the radiated sound pressure, ∇ is the Laplacian operator, $\nabla^2 = \frac{\partial^2}{\partial x^2} + \frac{\partial^2}{\partial y^2}$ for Cartesian coordinate system and $\nabla^2 = \frac{1}{r} \frac{\partial}{\partial r} r \frac{\partial}{\partial r}$ for cylindrical coordinate system, $\overrightarrow{r}$ is the position vector of receiving point R. By omitting the time-dependent term $e^{j\omega t}$, the solution to the above equation is:

$$p_{rad}(\overrightarrow{r}) = a H_0^{(2)}(kr), \tag{3}$$

where a is the amplitude determined by the strength of sound radiation source, $H_0^{(2)}$ is the zero order Hankel of the second kind.

Assuming the outlet aperture of a unit cell is small compared to the acoustic wavelength, and the receiving point R is located in the far field, the outlet aperture can be approximated as a point source with uniform velocity. The radiation strength is $a = k \rho_0 c_0 q/2$ and Eq. (3) can be further written as [23]:

$$p_{rad}(\overrightarrow{r}) = \frac{k \rho_0 c_0 q}{2} H_0^{(2)}(kr), \tag{4}$$

where q is to describe the strength of air velocity disturbance at the outlet aperture: $dq = \overline{u} dy$, with d here being the differential operator, $\overline{u}$ being the normal air velocity averaged over the aperture area h_o.

Assuming the radiated sound pressure field behind the baffle is a linear superposition of the sound fields generated by all the periodic unit cells. The sound pressure p_n at a specific unit cell n due to excitation from all the unit cells, including cell n itself, inversely affects the pressure continuity relation. This coupling effect has to be apprehended to solve the coupled system response. The mutual radiation impedance between a receiving unit cell n and an exciting unit cell m is $Z_{nm} = p_n/\overline{u}_m$, and the self-radiation impedance is $Z_{mm} = p_m/\overline{u}_m$. By translating the origin of the coordinate system to the center of the outlet aperture at the exciting cell m, i.e., let $y = 0$, the acoustic pressure on the receiving cell n due to an exciting cell m, provided that $m \neq n$ is:
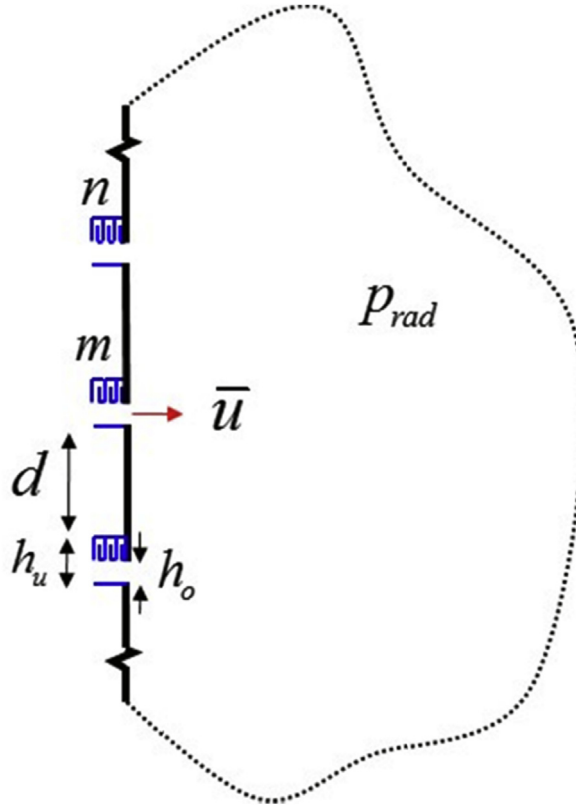
Fig. 2. Sound radiation from unit cell apertures into a semi-infinite free space.

$$p_n(y_n) = \frac{k\rho_0 c_0}{2} \int_{-h_o/2}^{h_o/2} \bar{u}_m H_0^{(2)}(ky)\mathrm{d}y, \tag{5}$$

where the integration is taken over the radiating outlet aperture at cell m from $-h_o/2$ to $h_o/2$. The mutual radiation impedance between cell m and n is thus:

$$Z_{nm} = \frac{p_n}{\bar{u}_m} = \frac{k\rho_0 c_0 h_o}{2} H_0^{(2)}(kd_{nm}), \tag{6}$$

where d_{nm} is the separation distance between the cell n and m.

For the self-radiation impedance where $m = n$:

$$Z_{mm} = \frac{p_m}{\bar{u}_m} = \frac{k\rho_0 c_0}{2} \int_{-h_o/2}^{h_o/2} H_0^{(2)}(ky)\mathrm{d}y. \tag{7}$$

The above equations are developed based on a two-dimensional system. It is worth noting that for a three-dimensional system with unit cells periodically arranged in a two-dimensional plane, another polar angle is needed to define the incident waves in Eq. (1) [24], and the radiation condition in Eqs. (6) and (7) should be rewritten using the Rayleigh's radiation integral. As a numerical example, the calculated radiation impedance, including real and imaginary parts of the self and mutual impedance, are plotted in Fig. 3. The size of the aperture h_o is 0.12 m and the distance d_{nm} is also 0.12 m.

The metamaterial unit cell is modeled as a waveguide to connect the incident and receiving sound fields analytically described as above. The sub-wavelength property of the unit cell makes it reasonable to consider its interaction with the adjacent acoustic fields as a one-dimensional waveguide. The cascaded coiled resonators in the side-branch generate accumulated effect on the sound transmission when sound propagates through a unit cell. For the metamaterial unit cell as shown in Fig. 1, its acoustic wave propagation in the duct is one-dimensional if the frequency range is below the cut-off frequency determined by the aperture size: $f_c = c_0/2h_o$. The one-dimensional waveguide can be described by the four-pole transfer matrix, which relates the pressure and velocity conditions on both ends of a unit cell as:
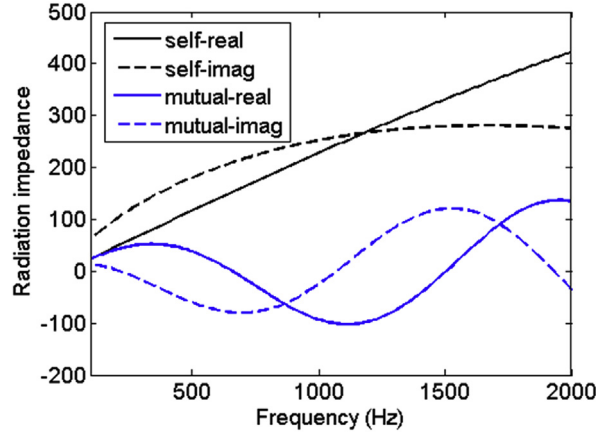
Fig. 3. The real and imaginary part of self and mutual radiation impedance, aperture size h_o is 0.12 m, distance d_{nm} is 0.12 m.

$$\begin{bmatrix} p_1 \\ u_1 \end{bmatrix} = \begin{bmatrix} A & B \\ C & D \end{bmatrix} \begin{bmatrix} p_2 \\ u_2 \end{bmatrix}. \tag{8}$$

The four-pole parameters can be obtained either analytically or numerically, depending on the complexity of the unit cell geometry. To use numerical method such as FEM, the conditions to be imposed at the unit cell boundaries and the parameters can be obtained are:

$$\begin{array}{l} u_2 = 0 : \begin{array}{l} A = p_1/p_2 \\ B = u_1/p_2 \\ p_2 = 0 : \begin{array}{l} C = p_1/u_2 \\ D = u_1/u_2 \end{array}. \end{array} \tag{9}$$

For a slab of acoustic grating composed of N periodic unit cells, the four-pole parameters for the identical unit cells are the same. At each unit cell, the sound pressure field on the incident side is a combination of the incident waves $\mathbf{p_{in}}$ and the reflected waves $\mathbf{Z}_r\mathbf{u_1}$, where $\mathbf{p_{in}}$ and $\mathbf{u_1}$ are $N \times 1$ vectors containing p_{in} and u_1 for each unit cell, $\mathbf{Z}_r$ is a $N \times N$ matrix containing the mutual- and self-radiation impedances calculated using Eq. (6)&(7). The transmitted sound field behind the structure is $\mathbf{Z}_r\mathbf{u_2}$. Note that the same representation of reflected and transmitted fields are considered here for the baffled condition, i.e., the reflected and transmitted fields are calculated using the same radiation impedance $\mathbf{Z}_r$. With the pressure continuity conditions, the coupled system can be written as [25]:

$$\begin{array}{l} \mathbf{p_{in}} - \mathbf{Z}_r\mathbf{u_1} = \mathbf{p_1} \\ \mathbf{Z}_r\mathbf{u_2} = \mathbf{p_2}. \end{array} \tag{10}$$

Together with the four-pole matrix relation for all the unit cells in Eq. (8), the entire system can be described by:

$$\begin{bmatrix} \mathbf{A} & \mathbf{B} & \mathbf{Z}_r \\ \mathbf{C} & \mathbf{D} & -\mathbf{I} \\ -\mathbf{I} & \mathbf{Z}_r & \mathbf{0} \end{bmatrix} \begin{bmatrix} \mathbf{p_2} \\ \mathbf{u_2} \\ \mathbf{u_1} \end{bmatrix} = \begin{bmatrix} \mathbf{p_{in}} \\ \mathbf{0} \\ \mathbf{0} \end{bmatrix}. \tag{11}$$

The system response can be solved once $\mathbf{u_1}$ and $\mathbf{u}_2$ are obtained. To calculate the STL, the sound power impinging on the slab is:

$$W_{in} = \frac{|p_0|^2}{2\rho_0 c_0} S_{slab} \cos \alpha, \tag{12}$$

where S_{slab} is the total area of the slab. The transmitted sound power from the slab is:

$$W_{trans} = \frac{1}{2} \int \text{Re}\left(p_{rad} \cdot \bar{u}^*\right) \mathrm{d}y = \frac{1}{2} \sum_1^N \text{Re}\left[(\mathbf{Z}_r \cdot \mathbf{u_2}) \cdot \mathbf{u_2}^*\right] h_0, \tag{13}$$

where the asterisk denotes the complex conjugate of the air velocity at the outlet aperture.

The STL of the acoustic grating is finally obtained as:

$$STL = 10 \log_{10}(W_{in}/W_{trans}),$$

(14)

which describes the sound insulation performance under baffled condition when the sound incidence is from a particular angle α. To perform diffuse field STL calculation, either the incidence angle can be swept from 0 to $\pi/2$ [22], or diffuse room with random sound incidence can be modeled to excite the structure [25].

3. One-dimensional acoustic transmission through a unit cell

We first analyze the acoustic transmission through a single unit cell and determine its effective material properties based on a simplified one-dimensional scenario. As shown in Fig. 4, the unit cell (with only one resonator layer) is placed in an acoustic duct whose height is identical to the unit cell height. The reflection and transmission relationship is studied using an impedance tube model to obtain the intrinsic property of the unit cell itself. Dimensions of the unit cell are sketched in Fig. 4(a). The unit cell height is 0.12 m, aperture height is 0.06 m, and the thickness for one resonator layer is 0.04 m. The coiled resonator has two parallel sub-chambers with identical thickness of 0.018 m. All boundary thicknesses are set as 0.002 m, which are assumed as rigid boundaries in the simulation. Vibro-acoustic coupling between thin walls and sound waves is neglected. At the duct left-end, plane wave sound incidence is defined and it travels towards the unit cell. Anechoic termination with a perfectly matched layer is applied at the right-end to prevent reflections. Given the current unit cell dimension, visco-thermal effect is also neglected (thus the system is linear and lossless). It should be noted that if the resonator channel is decreased down to millimeters, or if Helmholtz resonator effect is involved, visco-thermal loss is usually significant which needs to be carefully considered in the simulation [19,26].

The dispersion relation of the coiled resonator as shown in Fig. 4(a) is first numerically calculated using FEM by determining the eigenfrequencies of the unit cell for different wave-vector values within the first Brillouin zone. The Bloch wavenumber kw/π is displayed in Fig. 4(b), with $w = 0.04$ m being the thickness of the resonator. As the frequency approaches the band edge from below, the propagation of acoustic waves becomes highly dispersive, with the effective wavelength being greatly compressed. At higher frequency, a bandgap (shadowed area) can be observed where the acoustic waves are not propagative anymore. Hence, sound waves penetrating the metamaterial are strongly reflected. Next, a standard retrieval method is followed to extract the effective material properties from the reflection and transmission coefficient of the unit cell [27]. The impedance of the material Z is calculated as:
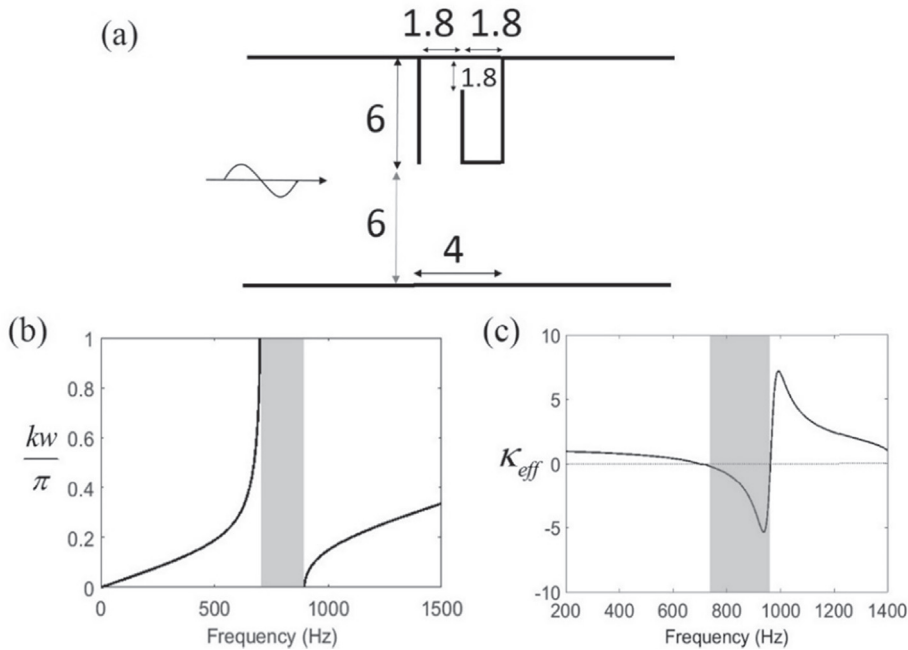

Fig. 4. (a) Dimensions of a single-layer coiled resonator, in cm. (b) The dispersion relation and (c) effective bulk modulus κ_{eff} calculated for the metamaterial unit cell.

$$Z = \frac{\mp\sqrt{\left(R^2 - T^2 - 1\right)^2 - 4T^2}}{1 - 2R + R^2 - T^2} \tag{15}$$

where R and T are the complex reflection and transmission coefficients containing the phase information. To obtain R and T, a standard impedance tube FEM model is employed to analyze the unit cell as shown in Fig. 4(a) [25]. The refraction index ξ can be calculated as:

$$\xi = \frac{-j\log\left[\left(1 - R^2 + T^2 \mp \sqrt{\left(R^2 - T^2 - 1\right)^2 - 4T^2}\right)\Big/ 2T\right] + 2\pi M}{kw}, \tag{16}$$

where w is the thickness of the unit cell and M is the branch number. A minimum thickness metamaterial that corresponds to $M = 0$ is used during the retrieval process [27,28]. The effective bulk modulus of the material and the effective mass density can then be obtained as:

$$\begin{aligned} \kappa_{eff} &= Z/\xi \\ \rho_{eff} &= Z\xi. \end{aligned} \tag{17}$$

In Fig. 4(c), the obtained effective bulk modulus κ_{eff} is plotted, which shows a region with negative parameter values from 700 to 950 Hz. The negative region arises from the local resonance of the coiled resonator. Along the wave propagation direction, additional resonator layers can be cascaded to broaden the attenuation bandwidth, as illustrated in Fig. 5. It has been discussed that there exists the so-called *Bragg* stop-band and *scatterer resonance* stop-band in such periodic waveguide (each coiled resonator is a scatterer) [29,30]. The *Bragg* stop-band is formed due to the interactions between scatterers (thus determined by their periodicity), whereas the *scatterer resonance* stop-band is caused by resonance induced sound reflection and features sharp attenuation peak. Since the coiled resonators are adjacent to each other, the band structure here is attributed to the *scatterer resonance* stop-band. Theoretically, infinite resonator layers can be cascaded to generate complete acoustic stop-band. However, only limited resonator layers are allowed in reality and the acoustic grating is preferable to be thin. In Fig. 5, the transmittance characteristics of a unit cell with different resonator layers are plotted. From one to four layers, the frequencies where the transmittance dip occurs generally remain the same, meaning the inherent effective property of the metamaterial is unchanged. The attenuation bandwidth with low transmittance is however enlarged with more layers. To effectively block sound transmission, we generally consider a transmittance of lower than 0.2 to be adequate. Therefore three resonator layers are chosen for a unit cell, as a trade-off between total thickness and attenuation bandwidth. The outer dimension of a unit cell is therefore 0.12 m by 0.12 m.

The final unit cell geometry is sketched in Fig. 6(a), and the one-dimensional STL of the unit cell with duct termination on both ends is shown in Fig. 6(b). The STL curve shows a sharp peak between 700 and 900 Hz with attenuation greater than 5 dB. The size of the unit cell (both height and thickness equal to 0.12 m) is about 0.27 of the acoustic wavelength at the main working frequency near 780 Hz, i.e., 0.27 λ, demonstrating a sub-wavelength character. The four-pole parameters of the unit cell obtained using Eq. (9) are presented in Fig. 7, which will be used subsequently to calculate the baffled STL of the periodic grating. Overall, the unit cell demonstrates sub-wavelength stop-band due to strong resonances incurred by the decorated resonators, which leads to nearly total sound reflection between 700 and 900 Hz. The frequency and bandwidth of the stop-band can be effectively tuned by designing the unit cell geometry upon incorporating systematic design schemes [31].
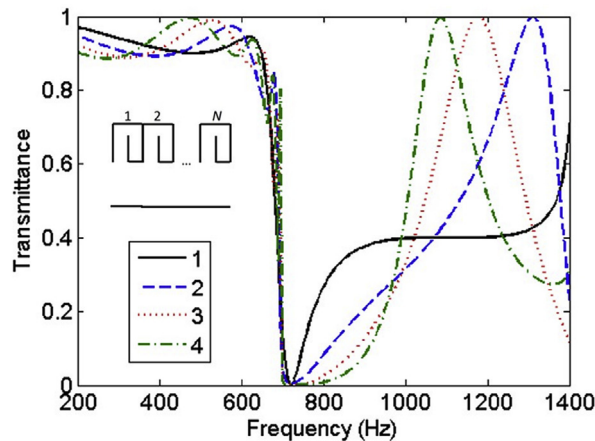

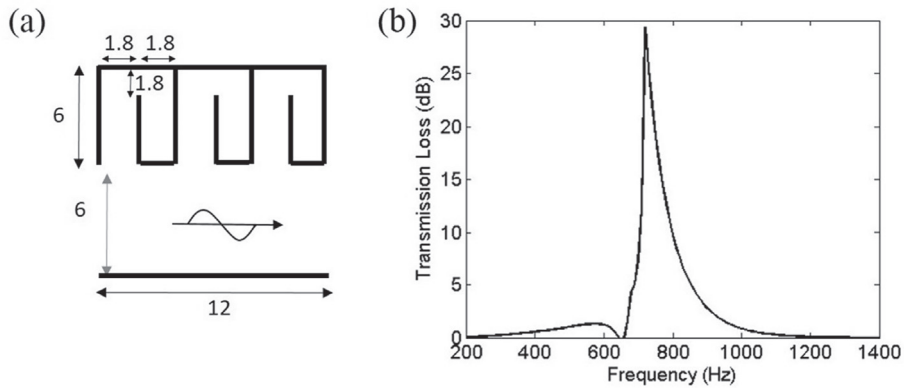**Fig. 5.** Transmittance of a unit cell with multiple layers of coiled resonators.

Fig. 6. (a) Unit cell geometry with three coiled resonators (in cm) and (b) the one-dimensional sound transmission loss.
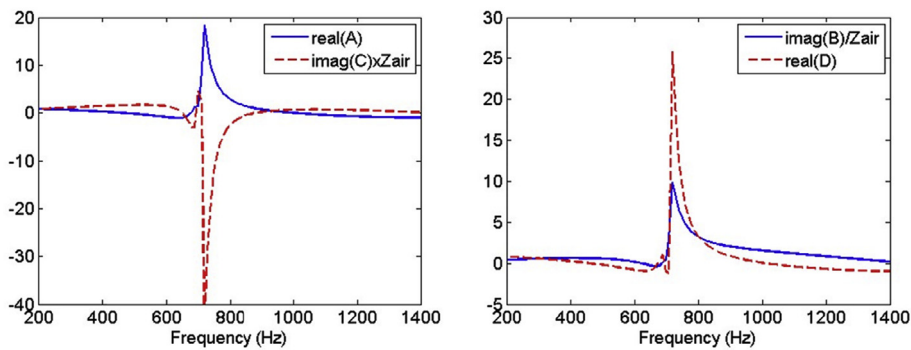

Fig. 7. The four-pole parameters of the unit cell obtained using Eq. (9).

Although purely reflective unit cells are investigated here, absorptive or hybrid unit cells [19,26] can be further explored to enrich the physical mechanism.

4. Numerical examples

4.1. Single unit cell

The STL of a single metamaterial unit cell on an infinite baffle is first investigated. Fig. 8 presents the STL calculated using the numerical approach as introduced in Sec. 2. The accuracy of the proposed approach was thoroughly validated against other simulation approaches such as FEM [25,32]. The STL results are presented for three sound incidence angles: normal $\alpha = 0°$, oblique $\alpha = 45°$ and $\alpha = 60°$, respectively. Generally, comparing to the duct-terminated unit cell STL in Fig. 6(b), the baffled STL shows more variations along the frequency range. The STL peak occurs in the same frequency between 700 and 900 Hz owing to the stop-band of the unit cell, which is as expected. However, at 500 Hz, the STL can drop down to negative values in Fig. 8 for all the three incidence angles. This was not found in the duct-terminated case.

To explain this, the only difference with the previous duct-terminated case is that the acoustic fields now are semi-infinite. This allows *edge diffraction* to occur when the wavelength of sound is longer or comparable to the size of the unit cell aperture. When edge diffraction happens, the unit cell behaves like an open acoustic duct connecting the two acoustic fields [33,34]. At the resonance, the *calculated* transmission coefficient can be greater than one, or, in another word, the STL can be negative valued. This is because edge diffraction leads to more energy transmit through the unit cell from the neighboring area, but the incident energy used for STL calculation, which is always taken over the same exposed area, is unchanged (see Eq. (14)). To qualitatively illustrate this, the sound pressure field and the intensity flow across the unit cell (represented by streamlines) are plotted at 500 Hz in Fig. 9, corresponding to the first dip in the STL curve in Fig. 8. Edge diffraction pattern in the incident field can be clearly observed with sound squeezing into the aperture, and the intensity flows are diffracted at the aperture edge. This results in more sound energy entering and transmitting through the aperture, numerically making W_{trans} greater than W_{in} (thus negative STL).
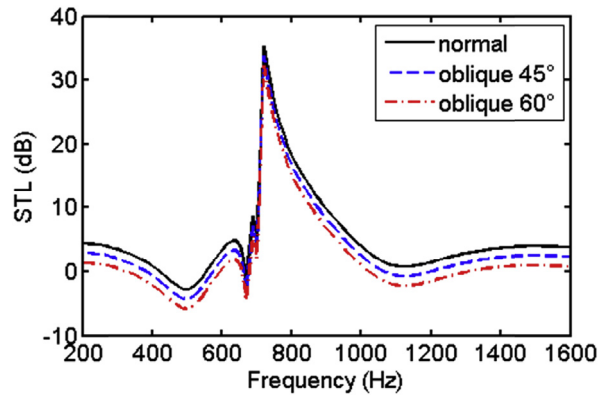
Fig. 8. STL of a single unit cell under normal or oblique sound incidence.

To quantify the diffraction effect, the STL of a duct-like aperture of size h_0 and thickness L' on a large baffle can be calculated using the following four-pore parameters:

$$\begin{bmatrix} p_1 \\ u_1 \end{bmatrix} = \begin{bmatrix} \cos(kL') & j\sin(kL')\rho_0 c_0 \\ j\sin(kL')/\rho_0 c_0 & \sin(kL') \end{bmatrix} \begin{bmatrix} p_2 \\ u_2 \end{bmatrix}. \tag{18}$$

For a duct-like aperture of size $h_o = 0.06$ m and thickness $L' = 0.12$ m, the calculated STL is plotted in Fig. 10. The predicted STL dip at 850 Hz however does not match with the metamaterial STL dip at 500 Hz. By examining the phase transition at the entrance of the metamaterial block in the pressure plot (Fig. 9), the coiled space in the resonator effectively elongate the duct thickness. After taking into account the coiled path and using an elongated effective thickness of $L' = 0.24$ m, the STL of a duct-like aperture is calculated, whose first two resonant dips (500 Hz and 1150 Hz) match well with the metamaterial STL. An alternative way to explain the observed phenomenon is by means of the so-called "slow sound" effect. As seen from the dispersion relation in Fig. 4(b), the effective wavelength within the metamaterial becomes compressed as the operating frequency approaches the stop-band from below, as a result of the strong dispersion [19,35]. Equivalently, the sound propagation speed within the metamaterial is slowed and the characteristic dimension (effective thickness of the structure) due to the coiled resonator is stretched. This matches with the previous numerical explanation. In sum, the major difference in the unit cell STL between one-dimensional condition (Fig. 6) and baffled condition (Fig. 8) is due to edge diffraction. The calculated STL using Eq. (14) can be negative at the diffraction dips induced by the resonance of the duct, and because of the "slow sound" effect, the effective wavelength within the metamaterial is compressed and the thickness of the structure is equivalently enlarged.

When the sound incidence is oblique, i.e., $\alpha = 45°$ and $60°$, the incident power is decreased by a factor of $\cos \alpha$ as indicated by Eq. (12). According to the STL definition in Eq. (14), this will cause the calculated STL under oblique incidence to be lower than the normal incidence case, which is as observed in Fig. 8. The shape of the STL curve is however unchanged because the unit cell reacts locally as a one-dimensional waveguide on the baffle. This assumption remains valid until the cut-off frequency is reached when $f_c = 343/0.06 = 5700$ Hz, which is much higher than the frequency of interest here. Generally, the metamaterial unit cell provides high sound insulation effect near its stop-band frequency as determined in Sec. 3, where the
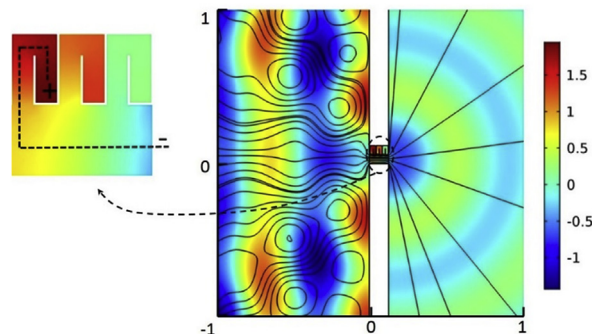

Fig. 9. Sound pressure field and intensity flow (represented by streamlines) at 500 Hz. Edge diffraction pattern in the incident field can be observed.
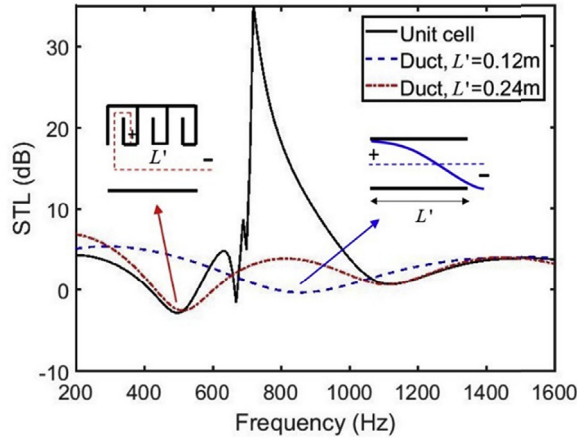
Fig. 10. The STL dips at 500 Hz and 1150 Hz due to edge diffraction match with the STL of a duct-like aperture on the baffle.

STL peak can exceed 30 dB in prediction. The single unit cell STL under baffled condition is also dependent on the sound incidence angle.

4.2. Metamaterial grating under normal sound incidence

The acoustic grating system comprised of five identical unit cells is investigated in this section. First, we consider normal sound incidence and study the effect of periodicity by varying the separation distance d (refer to Fig. 2). With $d = 0$ m, i.e., the unit cells are closely adjacent to each other, the grating's STL in Fig. 11 is more flattened compared to the single unit cell STL. The 5-cell grating does not show significant diffraction induced STL dip, and its STL is closer to the one-dimensional duct-terminated STL in Fig. 6. This is because the diffraction effect becomes less obvious as the filling ratio of grating elements increases. When d is increased to 0.12 m, the diffraction induced dip appears again, and gently moves to higher frequency comparing to the single unit cell curve. Interestingly, a new STL peak rises from 1300 Hz to 1500 Hz with $d = 0.12$ m. This was not found in the previous two cases with a single unit cell or $d = 0$ m.

The formation of the new high STL region can be explained by the *destructive radiation inference* among the periodic unit cells. To explain this, an idealized sound radiation model is illustrated in Fig. 12, where the outlet apertures of the periodic grating elements are simplified as an array of point radiators. The separation distance between two radiators, denoted as one period b, is $b = d + h_u$, with h_u being the unit cell size. For each single radiator, the radiated sound pressure at a receiving point R is:

$$p_i(\omega, r_i) = \frac{a}{\sqrt{r_i}} e^{j(\omega t - k r_i)} \tag{19}$$
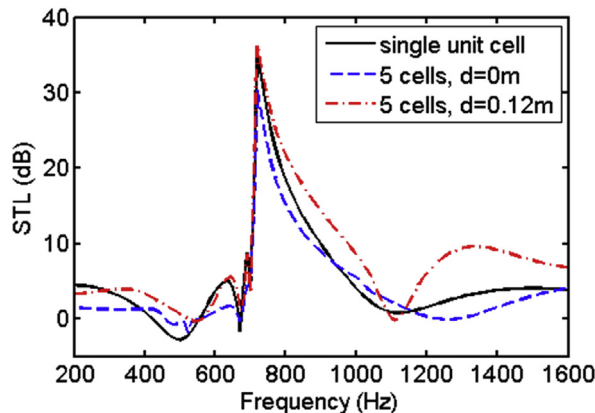

Fig. 11. Comparison between STL of a single unit cell and acoustic grating comprised of five unit cells with separation distance $d = 0$ m and $d = 0.12$ m.
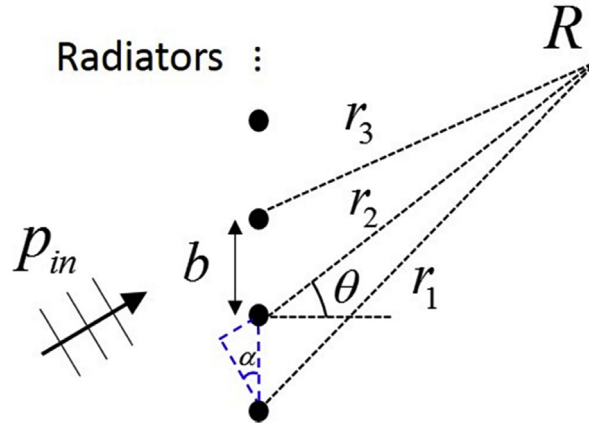
Fig. 12. The aperture outlets of the periodic grating elements are simplified as an array of point radiators to explain the radiation interference effect.

where r_i is the separation distance between the i-th source radiator and the receiving point. a is the pressure amplitude determined by the strength of sound source.

Assuming the receiving point is in the far field, the distance relative to the radiators can be approximated by:

$$
\begin{aligned}
r_2 &= r_1 + b \sin \theta \\
&\cdots \\
r_N &= r_1 + (N-1)b \sin \theta
\end{aligned}
\tag{20}
$$

The sound pressure at the receiver point R as a result of the super-positioned sound field due to an array of radiators is:

$$
\begin{aligned}
p(\theta,\omega,r) &= \frac{a}{\sqrt{r}}e^{j(\omega t - kr_1)}\left[1 + e^{-jkb\sin\theta} + \cdots + e^{-jk(N-1)b\sin\theta}\right] \\
&= \frac{a}{\sqrt{r}}e^{j(\omega t - kr_1)}\left[\frac{1 - e^{-jNkb\sin\theta}}{1 - e^{-jkb\sin\theta}}\right] \\
&= \frac{a}{\sqrt{r}}e^{j(\omega t - kr_1)}e^{-jNkb\sin\theta/2}e^{jkb\sin\theta/2}\left[\frac{e^{jNkb\sin\theta/2} - e^{-jNkb\sin\theta/2}}{e^{jkb\sin\theta/2} - e^{-jkb\sin\theta/2}}\right] \\
&\approx \frac{a}{\sqrt{r}}e^{j(\omega t - kr)}\frac{\sin(Nkb\sin\theta/2)}{\sin(kb\sin\theta/2)}
\end{aligned}
\tag{21}
$$

To determine the sound radiation pattern, the source strength term a can be normalized. The directivity pattern can then be derived from Eq. (21):

$$
D(\theta,\omega) = \frac{p(\theta,\omega)}{p(0,\omega)} = \left|\frac{\sin(Nkb\sin\theta/2)}{N\sin(kb\sin\theta/2)}\right|,
\tag{22}
$$

where $D(\theta,\omega)$ describes the strength of sound radiation in a specific angle θ relative to the normal angle $p(0,\omega)$. $D(\theta,\omega)$ in Eq. (22) is a function of the grating periodicity N and b, frequency k and radiation angle θ.

The radiated sound power to the far field is:

$$
W(\omega) = \int_{-\frac{\pi}{2}}^{\frac{\pi}{2}} N^2 D(\theta,\omega)^2 \mathrm{d}\theta = \int_{-\frac{\pi}{2}}^{\frac{\pi}{2}} \left|\frac{\sin(Nkb\sin\theta/2)}{\sin(kb\sin\theta/2)}\right|^2 \mathrm{d}\theta
\tag{23}
$$

Using the expression in Eq. (23), the radiation intensities (power normalized by surface) in decibels with unit cell distance $d = 0$ m, 0.15 m, and 0.3 m are plotted in Fig. 13(a). With unit cell size $h_u = 0.12$ m, the corresponding radiator periods are $b = 0.12$ m, 0.27 m, and 0.42 m, respectively. For $d = 0$ m, the radiation intensity is a continuously descending line in the interested frequency range. When d is increased to 0.15 m, the radiation intensity shows one trough at 1100 Hz, and the curve with $d = 0.3$ m shows two troughs at 650 Hz and 1500 Hz, respectively. Comparing to the baseline curve with $d = 0$ m, the destructive interference can significantly alter the radiation strength and thus sound transmission by more than 5 dB. In Fig. 13(b), the STLs of the acoustic grating with 5 unit cells are plotted for the three separation distances. The frequencies
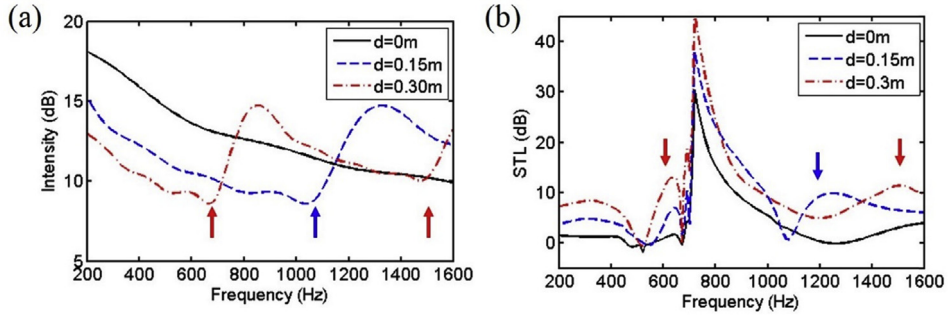
Fig. 13. (a) Sound radiation intensity of five radiators separated by different distances. (b) STLs of acoustic grating comprising 5 unit cells with different separation distance *d*. Arrows denote radiation valleys and attenuation peaks due to destructive interference.

where STL curve rises (marked by arrows) correlate well with those valleys in the intensity curve in Fig. 13, meaning the radiation deficiencies are transferred to those increments in the STL curves.

A more comprehensive illustration of the effect of destructive interference can be found in Fig. 14, where both variations of radiation intensity and STLs of the metamaterial grating are plotted against varying distance *d*. In Fig. 14(a), two canyons can be identified from the intensity plot, corresponding to the radiation modes where radiation levels are reduced due to destructive interference. The reduction is transferred into the enhanced attenuation regions as observed from Fig. 14(b). Note that the colormaps in the two figures are purposely reversed to show this relationship. With larger separation distance, the destructive interference region is shifted left towards lower frequencies. Between 700 and 950 Hz, the stop-band region with high STL levels can be clearly identified from the STL map. As the destructive interference can overlap with the acoustic stop-band in the frequency domain, the interference-induced STL increases may not exactly follow the intensity canyons in the frequencies and decibel values. Overall, Fig. 14 clearly demonstrates the effect of destructive inference as a result of the acoustic coupling between unit cells, which are periodically arranged in the direction normal to the sound propagation direction (tangent to the periodic grating).

Equation (22) can be applied to determine the directivity of the transmitted sound through the acoustic grating. For illustration purpose, the directivity pattern for the case with *d* = 0.3 m is calculated at 650 Hz and 1500 Hz, corresponding to the two troughs in the radiation power curve. Fig. 15 (left) shows the directivity polar plot at 650 Hz, where the main radiation direction is normal to the slab. The sound pressure distribution in the areas surrounding the acoustic grating is calculated and displayed on the right, which matches with the directivity obtained analytically using Eq. (22). Note that the polar plot only considers the radiation part (simplified using radiators), whereas the sound pressure distribution shows the fully coupled system response. At the second trough at 1500 Hz, directivity polar plot in Fig. 16 shows that the radiated sound field is scattered and indicates three distinct radiation angles. The sound pressure distribution plot of the coupled system again follows the simplified radiator model.

In sum, the normal incidence results show that acoustic metamaterial grating exhibits high transmission loss at its acoustic stop-band, and the periodic arrangement in the direction normal to the incidence leads to additional STL peaks formed owing to the destructive interference among those unit cells. The sound attenuation as a combined result of sound reflection and interference can be flexibly tailored via designing the system parameters. The transmitted sound depends on the unit cell geometry (as detailed in Sec. 3), the periodicity (number of unit cells *N* and distance between unit cells *d*), and the position of the observation point.
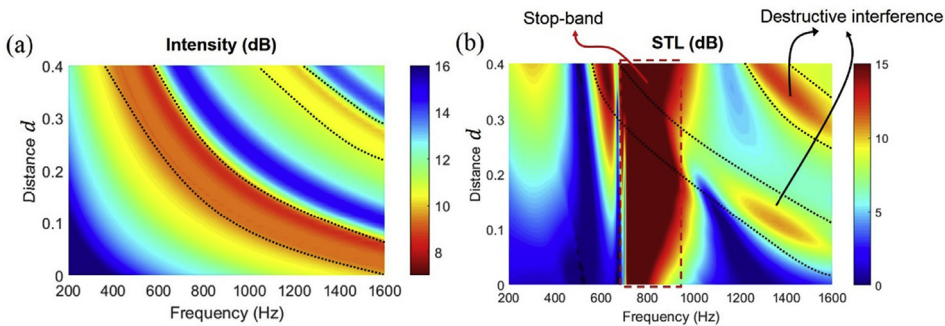

Fig. 14. (a) Variation of radiation intensity predicted using Eq. (23) with respect to different separation distance *d*. (b) STL of the acoustic grating with varying separation distance *d*. The stop-band and destructive interference regions can be clearly identified.
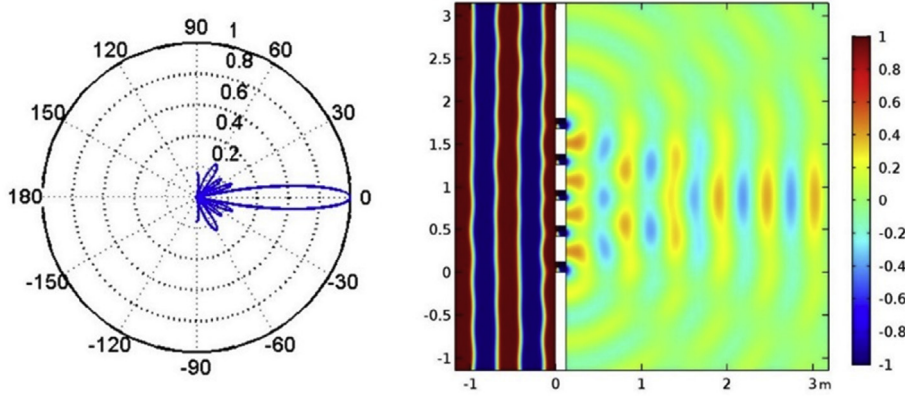
Fig. 15. The radiation directivity predicted using Eq. (22) (polar plot) and the sound pressure distribution in the coupled system at 650 Hz, $d = 0.3$ m, normal incidence.
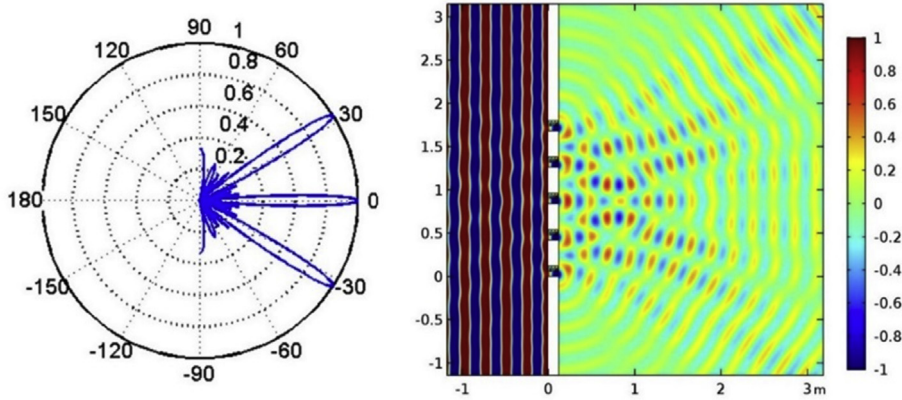

Fig. 16. The radiation directivity predicted using Eq. (22) (polar plot) and the sound pressure distribution in the coupled system at 1500 Hz, $d = 0.3$ m, normal incidence.

4.3. Metamaterial grating under oblique sound incidence

When the sound incidence is oblique in an angle α relative to the slab normal, the grating elements in the acoustic slab involve extra phase difference term, which could further change the sound radiation characteristics. The phase difference can be equivalently described using a time delay term in the radiators array model in Fig. 12. Consider the unit cells distributed in the y-axis are excited in sequence, their time delay can be described as:

$$\Delta t = (N - 1)b \sin \alpha / c_0 \tag{24}$$

Adding the time delay term into Eq. (19), the received sound pressure in the far field due to a radiating cell N is:

$$p_i(\theta, \alpha, \omega, r_i) = \frac{a}{\sqrt{r_i}} e^{j\{\omega[t-(N-1)b \sin \alpha/c_0]-kr_i\}} \tag{25}$$

Following the derivation in Eq. (21), the total sound pressure field due to N grating elements with period b is:

$$p(\theta, \alpha, \omega, r) = \sum_1^N p_i(\theta, \alpha, \omega, r_i) = \frac{a}{\sqrt{r}} e^{j(\omega t - kr)} \frac{\sin\left[\frac{Nkb}{2}(\sin \theta + \sin \alpha)\right]}{\sin\left[\frac{kb}{2}(\sin \theta + \sin \alpha)\right]}. \tag{26}$$

The directivity of sound radiation is changed to:

$$D(\theta, \alpha, \omega) = \left| \frac{\sin\left[\frac{Nkb}{2}(\sin\theta + \sin\alpha)\right]}{N\sin\left[\frac{kb}{2}(\sin\theta + \sin\alpha)\right]} \right|. \tag{27}$$

Hence, the radiated sound power describing interference between unit cells can be described as:

$$W(\alpha, \omega) = \int_{\frac{-\pi}{2}}^{\frac{\pi}{2}} N^2 D(\theta, \alpha, \omega)^2 d\theta = \int_{\frac{-\pi}{2}}^{\frac{\pi}{2}} \left| \frac{\sin\left[\frac{Nkb}{2}(\sin\theta + \sin\alpha)\right]}{\sin\left[\frac{kb}{2}(\sin\theta + \sin\alpha)\right]} \right|^2 d\theta. \tag{28}$$

Using the above equation, the frequency-dependent sound radiation intensity for the five radiators with two oblique cases ($\alpha = 20°$ and $30°$) are calculated and plotted in Fig. 17(a), where the separation distance is $d = 0.3$ m ($b = 0.42$ m). Again, the interference-induced variation in the radiation intensity curve is very significant. For example, at 650 Hz, the radiation intensity for the oblique case is 5 dB stronger than the normal case. This weakens the attenuation band formed previously due to destructive interference, as seen from the STLs of the acoustic gratings in Fig. 17(b). For all three cases, the main STL peak due to the acoustic stop-band occurs at the same frequency (780 Hz), and the peak level is slightly weakened with oblique incidence.

For more general comparison, Fig. 18(a) presents the variation of radiation intensity with respect to sound incidence angle α predicted using Eq. (28). Instead of showing two smooth canyons as compared to Fig. 14(a), the effect of incidence angle seems to be more complex. A few regions with reductions in radiation levels can be identified following the prescribed lines, and they are reflected as STL increases in Fig. 18(b). Using $\alpha = 0°$ as the benchmark, increasing incidence angle α from $0°$ to $60°$ weakens the destructive interference and lowers the attenuation peaks induced by this effect. The frequency is also shifted lower. This confirms that destructive interference due to couplings between grating elements is sensitive to the angle of incidence. The stop-band region is again minimally affected by the destructive interference.

From the numerical results, the major factors affecting the STL performance of the baffled metamaterial grating system are summarized as follows: (i) the acoustic property of the metamaterial unit cell, which depends on its design geometry and the mechanism inducing the acoustic stop-band; (ii) edge diffraction effect when the wavelength of sound is comparable to the size of the unit cell opening; and (iii) the destructive interference behind the baffle, which is in general dependent on the periodicity of the metamaterial grating and the sound incidence angle. It can be anticipated that to construct metasurface
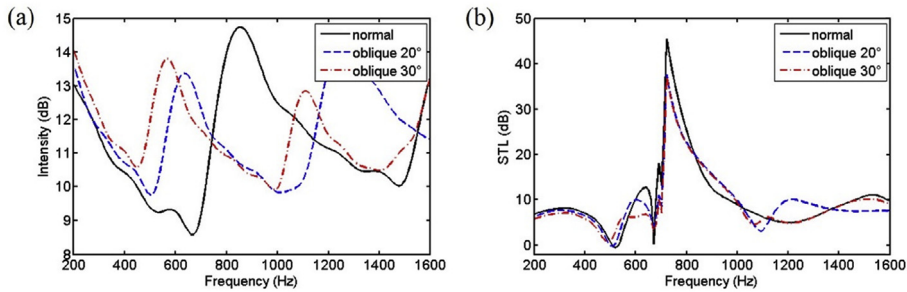

Fig. 17. (a) Sound radiation intensity of five radiators with oblique incidences $\alpha = 20°$ and $30°$, the separation distance is $d = 0.3$ m; (b) STL of the acoustic grating under normal and oblique sound incidence.
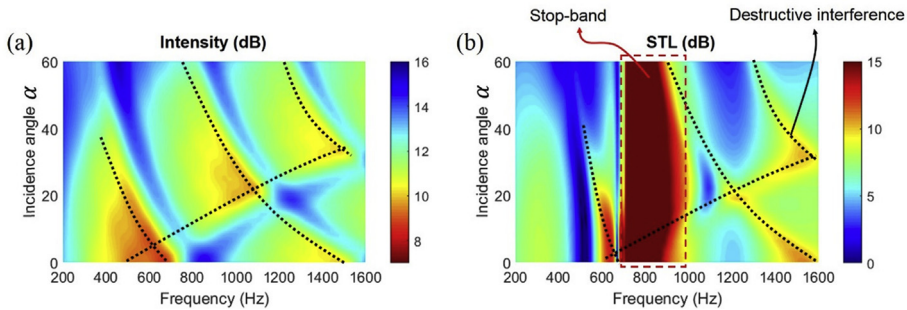

Fig. 18. (a) Variation of radiation intensity with respect to sound incidence angle α predicted using Eq. (28); (b) STL of the acoustic grating with varying incidence angle α.

with phase tailoring functionality [32], the analytical equation as derived in Eq. (28) can be extended with extra terms to describe the phase shift property within the unit cells.

5. Experimental validation

To validate the proposed numerical approach, an experimental test was performed using a two-dimensional acoustic plane as illustrated in Fig. 19. The height of the acoustic plane is set as 0.05 m, and five identical unit cells are closely connected together ($d = 0$ m) to form an acoustic grating. The experiment considers a 1:2 scale model, with the dimension of each unit cell in Fig. 6(a) being reduced by half (to 0.06 × 0.06 m). The size of the experimental system is limited by the 3D printing technology used for fabricating unit cells. The single-layer slab thus has a thickness of 0.06 m and a total length of 0.06 × 5 = 0.3 m, as sketched in Fig. 20. The unit cells are joined together and fixed to the setup using mounting tape.

The sound source is a loudspeaker attached to a duct with a dimension of 0.9 × 0.3 × 0.05 m, which generates normal acoustic excitation to the slab. The duct is to facilitate a measurement of the incident sound power, although plane wave condition is not fully guaranteed when the measurement frequency exceeds the duct cut-off frequency. Also, the reflected sound field may differ from the free-radiation condition as modeled in the simulations. At the receiving side, the outlet plane has a dimension of 1.2 × 0.94 × 0.05 m, which is treated with acoustic wedges to minimize reflections from the boundary. Three PCB array microphones (model 130E20) were used for measuring the sound pressure in the 2D plane. 'Mic.1' and 'Mic.2' were flush-mounted on the source duct to identify the incident and reflected sound wave, and 'Mic.3' is used to measure the outlet sound pressure along a semicircular path of radius 0.4 m. All the acquisition and control signals were controlled based on a NI PXI platform. The unit cells were fabricated using 3D printing technology on a Stratasys FORTUS 250 MC printer with acrylonitrile butadiene styrene (ABS) additive. The printing thickness for the unit cell walls was set as 1 mm, thus one can expect vibro-acoustic coupling effect between the sound waves and thin walls, which could influence the STL performance of the structure. The printed unit and the testing facility are shown in Fig. 20.

Fig. 21 compares the predicted and measured STL for the constructed metamaterial acoustic grating from 400 Hz to 2800 Hz. Generally, a good agreement is observed between the shape of the predicted and experimental curves. The discrepancies can be caused by a few plausible reasons such as the difference in the sound incidence and radiation conditions, geometric imperfection and experimental error. The predicted STL peak (near 50 dB) is higher than the experimental value (at 40 dB), which could be possibly attributed to the vibro-acoustic coupling effect as explained above. The measured STL band over 10 dB is wider than the predicted one, possibly due to the neglected visco-thermal effect and vibro-acoustic coupling. Overall, the experiment validates the proposed approach and demonstrates the sound isolation capacity of the device. The experimental conditions can be further refined, and the visco-thermal and vibro-acoustic effects can be taken into account in future studies to improve the accuracy.
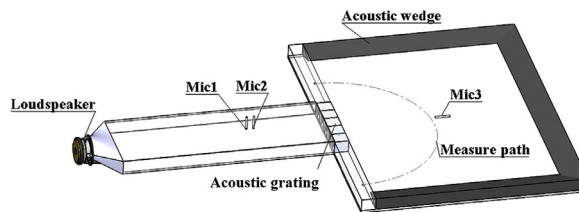

Fig. 19. Experimental set-up to measure the STL of an acoustic grating composed of periodic unit cells.
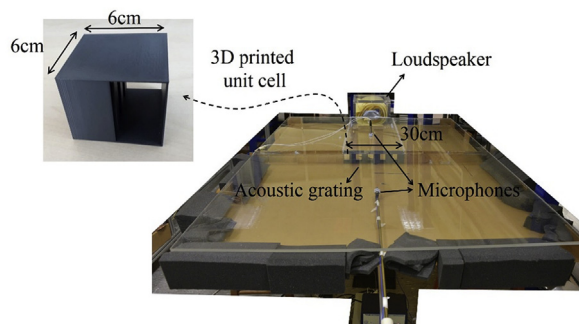

Fig. 20. Photo of the 3D printed unit cell and the experimental test-rig.
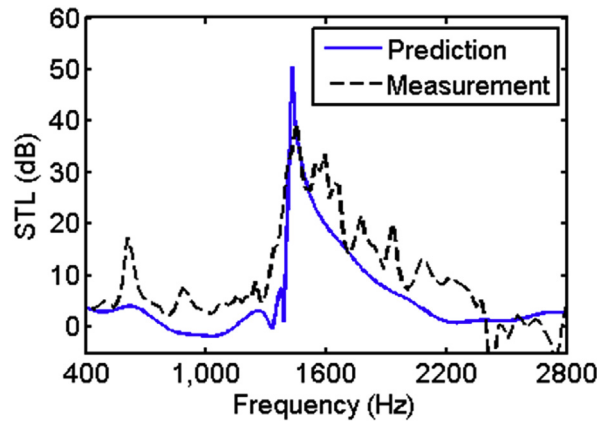
Fig. 21. Comparison between predicted and measured STL for the acoustic grating comprising 5 identical unit cells.

6. Conclusions

This paper has presented an investigation on the sound transmission through an acoustic grating system comprised of sub-wavelength unit cells. The unit cell was constructed based on an acoustic duct decorated with coiled resonators. A number of unit cells were arranged periodically in a slab to form an acoustic grating, aiming to provide sound insulation in the design frequency range without entirely blocking the air transportation.

The metamaterial property of the unit cell has been analyzed using a simplified one-dimensional model (Sec. 3), showing high dispersion relation, negative effective material property and sub-wavelength character. Using the standard retrieval method, the obtained effective bulk modulus showed a negative region, which causes strong sound reflection at the unit cell. With more layers of resonators, the sound reflection can be enhanced and broadened to wider frequencies. The chosen unit cell comprised of three coiled resonators has a dimension of 0.12 × 0.12 m. Its size is about a quarter of the wavelength at its stop-band frequency.

An analytical approach has been proposed to predict the STL of the acoustic grating under baffled condition (Sec. 2). The mechanism study (Sec. 4) has discovered three main physical effects which affect the STL response, including the acoustic stop-band, edge diffraction and destructive radiation interference. Their effects can be summarized in the following:

1) The sharp STL peak where sound transmission is strongly prohibited is attributed to the stop-band property of the unit cell. Baffled condition does not vary this stop-band compared to the one-dimensional duct condition. To obtain a slab structure with high sound isolation in a desired frequency range, the unit cell geometry can be tuned and optimized.
2) When the aperture size of the unit cell is smaller than the acoustic wavelength, edge diffraction can cause a unit cell to be acoustically transparent. At the diffraction frequency, the unit cell behaves like a resonant open duct on the baffle. The characteristic thickness of the duct is enlarged due to high dispersion or "slow sound" effect within the metamaterial unit cell.
3) Destructive radiation interference among the periodic unit cells creates additional attenuation peaks. The interference relationship is frequency-dependent, which highly depends on the grating periodicity and the angle of incidence. A simplified model based on an array of radiators was derived to characterize such effect analytically.

The validity of the proposed numerical approach was verified experimentally, which successfully captured high sound reduction (close to 40 dB) in the experiment. This study indicates that sound transmission in an acoustic grating can be flexibly tuned or on-demand controlled by proper tuning of the unit cell geometry and periodicity of the grating elements. For such purpose, the physical aspects as detailed in this study could provide theoretical guidelines, and the proposed numerical approach serves as an efficient design tool. Promising applications including ventilation windows or noise barriers for noise mitigation can be anticipated from this study. It is worth noting that the unit cells constituting the slab structure can be endowed with phase tailoring functionality to form an acoustic metasurface. The proposed modeling framework can be readily extended to metasurface studies.

Appendix A. Supplementary data

Supplementary data to this article can be found online at https://doi.org/10.1016/j.jsv.2019.02.042.

References

[1] M.R. Haberman, M.D. Guild, Acoustic metamaterials, Phys. Today 69 (6) (2016) 42–48.
[2] G. Ma, P. Sheng, Acoustic metamaterials: from local resonances to broad horizons, Sci. Adv. 2 (2016), e1501595.
[3] S.A. Cummer, J. Christensen, A. Alù, Controlling Sound with Acoustic Metamaterials, vol. 1, 2016, p. 16001.
[4] Z. Liu, X. Zhang, Y. Mao, Y.Y. Zhu, Z. Yang, C.T. Chan, P. Sheng, Locally resonant sonic materials, Science 289 (5485) (2000) 1734–1736.
[5] Z. Yang, J. Mei, M. Yang, N.H. Chan, P. Sheng, Membrane-type Acoustic metamaterial with negative dynamic mass, Phys. Rev. Lett. 101 (20) (2008), 204301.
[6] N. Fang, D. Xi, J. Xu, M. Ambati, W. Srituravanich, C. Sun, X. Zhang, Ultrasonic metamaterials with negative modulus, Nat. Mater. 5 (6) (2006) 452–456.
[7] M.S. Kushwaha, P. Halevi, L. Dobrzynski, B. Djafari-Rouhani, Acoustic band structure of periodic elastic composites, Phys. Rev. Lett. 71 (13) (1993) 2022–2025.
[8] Y. Chen, G. Huang, X. Zhou, G. Hu, C.-T. Sun, Analytical coupled vibroacoustic modeling of membrane-type acoustic metamaterials: membrane model, J. Acoust. Soc. Am. 136 (3) (2014) 969–979.
[9] F. Langfeldt, J. Riecken, W. Gleine, O. von Estorff, A membrane-type acoustic metamaterial with adjustable acoustic properties, J. Sound Vib. 373 (Supplement C) (2016) 1–18.
[10] F. Langfeldt, W. Gleine, O. von Estorff, Analytical model for low-frequency transmission loss calculation of membranes loaded with arbitrarily shaped masses, J. Sound Vib. 349 (Supplement C) (2015) 315–329.
[11] G. Ma, M. Yang, S. Xiao, Z. Yang, P. Sheng, Acoustic metasurface with hybrid resonances, Nat. Mater. 13 (9) (2014) 873–878.
[12] Y. Cheng, C. Zhou, B.G. Yuan, D.J. Wu, Q. Wei, X.J. Liu, Ultra-sparse metasurface for high reflection of low-frequency sound based on artificial Mie resonances, Nat. Mater. 14 (10) (2015) 1013–1019.
[13] X. Wu, C. Fu, X. Li, Y. Meng, Y. Gao, J. Tian, L. Wang, Y. Huang, Z. Yang, W. Wen, Low-frequency tunable acoustic absorber based on split tube resonators, Appl. Phys. Lett. 109 (4) (2016), 043501.
[14] Y. Xie, W. Wang, H. Chen, A. Konneker, B.-I. Popa, S.A. Cummer, Wavefront modulation and subwavelength diffractive acoustics with an acoustic metasurface, Nat. Commun. 5 (2014).
[15] Y. Li, X. Jiang, R.-q. Li, B. Liang, X.-y. Zou, L.-l. Yin, J.-c. Cheng, Experimental realization of full control of reflected waves with subwavelength Acoustic metasurfaces, Phys. Rev. Appl. 2 (6) (2014), 064002.
[16] Y. Li, B. Assouar, Acoustic metasurface-based perfect absorber with deep subwavelength thickness, Appl. Phys. Lett. 108 (2016), 063502.
[17] V.M. García-Chocano, R. Graciá-Salgado, D. Torrent, F. Cervera, J. Sánchez-Dehesa, Quasi-two-dimensional acoustic metamaterial with negative bulk modulus, Phys. Rev. B 85 (18) (2012), 184102.
[18] K.J.B. Lee, M.K. Jung, S.H. Lee, Highly tunable acoustic metamaterials based on a resonant tubular array, Phys. Rev. B 86 (18) (2012), 184302.
[19] N. Jiménez, V. Romero-García, V. Pagneux, J.-P. Groby, Quasiperfect absorption by subwavelength acoustic panels in transmission using accumulation of resonances due to slow sound, Phys. Rev. B 95 (1) (2017), 014205.
[20] N. Jiménez, V. Romero-García, V. Pagneux, J.-P. Groby, Rainbow-trapping absorbers: broadband, perfect and asymmetric sound absorption by sub-wavelength panels for transmission problems, Sci. Rep. 7 (2017) 13595.
[21] Y. Xie, B.-I. Popa, L. Zigoneanu, S.A. Cummer, Measurement of a broadband negative index with space-coiling acoustic metamaterials, Phys. Rev. Lett. 110 (17) (2013), 175501.
[22] C. Wang, L. Huang, Y. Zhang, Oblique incidence sound absorption of parallel arrangement of multiple micro-perforated panel absorbers in a periodic pattern, J. Sound Vib. 333 (25) (2014) 6828–6842.
[23] P.R. Stepanishen, Acoustic two-dimensional radiation and scattering from cylinders using source density, SVD and Fourier methods, J. Sound Vib. 201 (3) (1997) 305–321.
[24] X. Wu, K.Y. Au-Yeung, X. Li, R.C. Roberts, J. Tian, C. Hu, Y. Huang, S. Wang, Z. Yang, W. Wen, High-efficiency ventilated metamaterial absorber at low frequency, Appl. Phys. Lett. 112 (10) (2018), 103505.
[25] X. Yu, Z. Lu, L. Cheng, F. Cui, On the sound insulation of acoustic metasurface using a sub-structuring approach, J. Sound Vib. 401 (2017) 190–203.
[26] A. Elayouch, M. Addouche, A. Khelif, Extensive tailorability of sound absorption using acoustic metamaterials, J. Appl. Phys. 124 (15) (2018), 155103.
[27] V. Fokin, M. Ambati, C. Sun, X. Zhang, Method for retrieving effective properties of locally resonant acoustic metamaterials, Phys. Rev. B 76 (14) (2007).
[28] D.R. Smith, S. Schultz, P. Markoš, C.M. Soukoulis, Determination of effective permittivity and permeability of metamaterials from reflection and transmission coefficients, Phys. Rev. B 65 (19) (2002), 195104.
[29] C.E. Bradley, Time harmonic acoustic Bloch wave propagation in periodic waveguides. Part I. Theory, J. Acoust. Soc. Am. 96 (3) (1994) 1844–1853.
[30] C.E. Bradley, Time harmonic acoustic Bloch wave propagation in periodic waveguides. Part II. Experiment, J. Acoust. Soc. Am. 96 (3) (1994) 1854–1862.
[31] X. Yu, Y. Tong, J. Pan, L. Cheng, Sub-chamber optimization for silencer design, J. Sound Vib. 351 (0) (2015) 57–67.
[32] J. Li, C. Shen, A. Díaz-Rubio, S.A. Tretyakov, S.A. Cummer, Systematic design and experimental demonstration of bianisotropic metasurfaces for scattering-free manipulation of acoustic wavefronts, Nat. Commun. 9 (1) (2018) 1342.
[33] M.C. Gomperts, T. Kihlman, The sound transmission loss of circular and slit-shaped apertures in walls, Acta Acustica united Acustica 18 (3) (1967) 144–150.
[34] D.J. Oldham, X. Zhao, Measurement of the sound transmission loss of circular and slit-shaped apertures in rigid walls of finite thickness by intensimetry, J. Sound Vib. 161 (1) (1993) 119–135.
[35] J.-P. Groby, W. Huang, A. Lardeau, Y. Aurégan, The use of slow waves to design simple sound absorbing materials, J. Appl. Phys. 117 (12) (2015), 124903.